Page 1 of 19. Royal Aeronautical Society 2018

Scale-Resolving Simulation of Shock Buffet Onset Physics on a Civil Aircraft Wing

Luke Masini
l.masini@liverpool.ac.uk
PhD Student
School of Engineering
University of Liverpool
United Kingdom

Sebastian Timme
sebastian.timme@liverpool.ac.uk
Senior Lecturer
School of Engineering
University of Liverpool
United Kingdom

Andrew J. Peace
apeace@ara.ac.uk
Chief Scientist
Computational Aerodynamics
Aircraft Research Association
United Kingdom

ABSTRACT

Transonic shock buffet on civil aircraft wings remains a key challenge for aerodynamicists, with no unequivocal explanation of the flow mechanisms governing buffet onset. This paper presents a delayed detached-eddy simulation of a large civil aircraft wing in the vicinity of buffet onset, set up to reproduce experimental flow data enabling direct comparisons. Besides conventional post-processing, the unsteady flow field is analysed using modal analysis techniques, including proper orthogonal decomposition and dynamic mode decomposition. Both methods reveal dominant modes pertaining to the shock buffet instability, showing outboard-running waves along the shock wave and the presence of buffet cells at a characteristic Strouhal number. Complementary experimental data from dynamic pressure-sensitive paint gives critical insight into the flow and a modal analysis of this dataset confirms the numerical observations. These high-quality datasets further the understanding of edge-of-the-envelope flow physics, ultimately informing modern wing design and buffet control strategies.

1.0 INTRODUCTION

Shock buffet is an aerodynamic instability that produces unsteady loads, consequently leading to structural excitation called buffeting. During transonic flight, shock-wave/boundary-layer interactions on the wing's surface induce boundary-layer separation at critical values of Mach number and angle of attack. This instability limits the flight envelope motivating continuous scrutiny from both industry and academia.

Extensive research since the 1950s has greatly improved the understanding of the two-dimensional (2D) case. Whilst various explanations for the self-sustained periodic shock motion have been reported, it is generally agreed that an acoustic feedback loop (1) sustains the shock motion on aerofoils. Low-frequency shock oscillations have been reported from several experimental (2–4) and numerical investigations (5–12), typically within a narrow frequency band between Strouhal numbers of 0.05 and 0.08 based on chord length, even though the propagation path of the acoustic waves remains contradictory. Numerical studies of aerofoil buffet are extensive, including unsteady Reynolds-averaged Navier-Stokes (RANS) simulations (5–7), detached-eddy simulations (DES), including the zonal (8) and the delayed (9) (DDES) approach, and large-eddy simulation (LES) (10). Buffet onset has also been linked to a global instability (11,12) providing an alternative explanation to the acoustic model.

Literature on the far more complex three-dimensional buffet on transport-type wings is more limited, with the elucidation of the governing flow physics remaining unclear. A number of research organisations have invested substantial resources into this topic, with their contributions reviewed recently (13). Early flight test data (14) and wind-tunnel testing (15–17) has indicated non-periodic shock motion with broadband frequency content, at a Strouhal number range of $0.2 \leq St \leq 0.6$, based on mean aerodynamic chord (MAC). Such studies point towards different physical mechanisms governing the 2D case, or infinite rectangular wings, and swept-wing geometries. Systematic studies focussing on the sweep angle effect have revealed contrasting mechanisms at low- and high-sweep angles, with the separated region moving closer to the wing tip with increasing sweep (17). Additionally, shock oscillations propagate pressure towards the wing tip via so-called buffet cells (18). Such behaviour has been reported on different wing geometries in various wind tunnels (19–21). Recent progress in global instability analysis has linked wing buffet cells to an unstable linear eigenmode (22,23).

Increasingly sophisticated experiments and numerical studies have significantly contributed to the understanding of the flow physics. The application of advanced optical techniques such as dynamic pressure-sensitive paint (DPSP) has been instrumental to visualise the flow at edge-of-the-envelope conditions. Early applications (24,25) were limited in terms of resolution and/or coverage, but more recent experiments (19,26) have been successful in revealing the flow structures. Such datasets are critical to validate increasingly complex numerical simulations, with the DES (5,27,28) approach showing capability to resolve the shock dynamics and propagation of buffet cells. Such massive datasets require effort to post-process, with the recent application of modal analysis techniques showing great potential in identifying the flow characteristics (29,30).

This paper presents a DDES study on a half wing-body configuration at buffet onset conditions. This work forms part of a larger effort that includes a state-of-the-art experimental dataset (19,29) and numerical simulations (22,27,31) of the same configuration. Whilst the flow at buffet onset and within the deep-buffet region has distinct characteristics and spectral content, the limited literature on wing buffet tends to focus on the cases well-beyond onset conditions. This study aims to bridge this gap by presenting a synergistic study complementing high-quality experimental and numerical data, together with modal analysis techniques to interrogate the inherent dynamics at buffet onset. Section 2 outlines the methodology, including the geometry, flow conditions and the numerical settings, followed by an overview of the analysis techniques. The main results from steady-state simulations and the DDES are presented in Section 3, with a detailed discussion of the flow unsteadiness from a phenomenal and quantitative comparison between different experimental and numerical studies.

2.0 METHODOLOGY

2.1 Geometry and Flow Conditions

The test case is a half wing-body configuration representing a commercial aircraft of a typical 1970s/1980s design. The geometry has been scaled down to wind tunnel dimensions, corresponding to the RBC12 wind tunnel half-model. The semi-span is 1.104 m and the MAC is 0.279 m. The wing is twisted and tapered, with an aspect ratio of 7.78, a constant quarter-chord sweep angle of 25° and leading-edge sweep angle Λ_{LE} of 28.3°. This configuration has been extensively tested at the Aircraft Research Association Transonic Wind Tunnel(19) and is the subject of previous numerical studies(22,27,31). The geometry is considered to be rigid, excluding any static deformation, which is believed to have negligible influence on the RBC12(19).

This simulation aims to reproduce the experimental aerodynamic flow field at buffet onset conditions. The rigid geometry assumption also excludes any structural or wind tunnel excitations, such that this study focusses exclusively on the inherent dynamics of shock buffet. The Mach number M_∞ is 0.8 while the reference temperature and pressure are 266.5 K and 66.0 kPa, respectively, resulting in a Reynolds number of 3.75 million based on MAC. Experimentally, at this Mach number buffet onset was defined at 2.7°, as indicated by several local and global criteria(19,29). Numerically, a critical angle of attack of around 3.0° has been obtained from URANS simulations(32) and a global stability analysis(22) when using the Spalart-Allmaras (S-A) model for turbulent closure. In the present simulation, the angle of attack was set at 3.1°.

Caution should be exercised when directly comparing experimental and numerical incidence angles. Experimental data(19,29) has been corrected for interference effects including wall constraint and paint influence in the case of incidence, and wind tunnel blockage for Mach number. Additionally, the flow may experience a small flow angle in the vicinity of a wind tunnel model, usually determined by inverting models. However, this is not an option with half-models mounted on the floor and the flow angle cannot be directly measured. Nonetheless, this was estimated to be around 0.35° for reference purposes, based on several other tests comparing half-models and sting-mounted full models. This estimate was not applied to the data unless otherwise stated.

Fixed transition was imposed numerically to replicate the wind tunnel test. On the suction surface, transition was fixed at 10% chord at the wing tip, 14% at the crank and 15% at the root, while this was 5% chord on the pressure side. Far-field conditions are applied at a distance of 25 semi-span lengths (around 90 MACs) while the wind tunnel floor is represented by a symmetry plane along the centre plane.

2.2 Numerical Approach

2.2.1 Flow Solver

The unstructured finite-volume solver TAU, developed by the German Aerospace Centre (DLR), was used to perform both steady-state and time-accurate simulations. In all cases, the second-order central scheme was applied to discretise the inviscid fluxes of the mean flow equations. Whilst scalar dissipation was used for steady RANS simulations, discretisation errors for the DDES were minimised by a second-order energy conserving skew-symmetric convection operator combined with a low-dissipative fourth-order matrix scheme(33). The turbulence model of choice was the negative S-A model(34). Concerning the convective fluxes of the turbulence model, a first-order Roe scheme was employed for RANS, whilst the second-order central scheme was used for the DDES. The first-order scheme better predicts the separated region for RANS solutions, but the choice of turbulence model discretisation becomes less critical for the DDES with low-dissipation(27,35). Gradients of the flow variables were reconstructed with a least squares approach which minimises errors in hybrid grids.

DDES with low-Reynolds-number correction(36) was chosen for the scale-resolving simulation, shielding the flow within the boundary layer from switching to LES mode. The recently developed hybrid-LD2 scheme(37) which blends the numerical parameters of the low-dispersive, low-dissipative scheme(38,39) with a more dissipative reference scheme was selected for robustness. Minimal dissipation was ensured by setting the inverse fourth-order dissipation coefficient to 256 for the reference scheme, and blends to 1024 in resolved vortex-dominated flow regions. Switching between RANS and LES regions was controlled by the maximum edge spacing.

Temporal discretisation was based on the standard second-order dual-time stepping approach. The physical time-step was set to 1 μs corresponding to a CFL number of $\mathcal{O}(1)$, using 1.5 times freestream velocity and the grid spacing in the focus region(40). A dynamic Cauchy convergence is applied for dual-time iterations, controlled by the drag coefficient with a relative error smaller than 10^{-8} within the last 20 iterations. Moreover, a minimum of 100 inner iterations are always performed such that the density residual converges to at least an order of magnitude.

2.2.2 Computational Mesh

The hybrid mesh was produced using the SOLAR mesh generator(41) generally following industry best-practice guidelines(42). A highly refined mesh consisting of $n = 50.4 \times 10^6$ points corresponding to 206.1×10^6 mixed elements of hexahedral, prism and tetrahedral type was generated to resolve the turbulent structures in the separated zone. Two large mesh sources for the LES focus regions were added to the standard sources of complex wing geometries, as depicted in Figure 1. The first extends from 60% span to just outboard of the tip in the spanwise direction, and covers the chordwise distance from just aft of the leading edge, to around 4 MACs downstream of the trailing edge, reaching the tail. The surface elements have a target spacing of $\Delta_0 \approx 0.0008$ m (0.003 MAC), where $\Delta_0 = max(\Delta_x, \Delta_y, \Delta_z)$. This region was informed by experimental analysis(19,29) and previous numerical simulations, which have shown that separation on this particular wing first occurs on outboard sections(22,27). The second source extends from the root to 60% span, and extends approximately

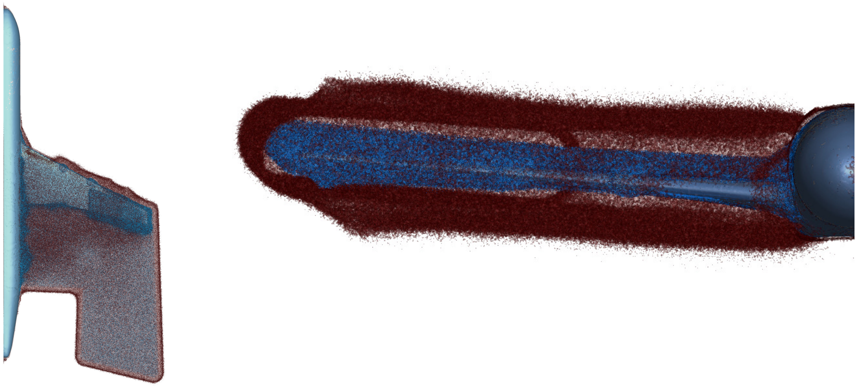

Figure 1. Mesh isovolumes highlighting the refinement by LES mesh sources. Isovolumes of size 5×10^{-9} m^3 shaded in blue; 5×10^{-8} m^3 shaded in red.

2 MACs downstream of the crank, producing surface elements of $\Delta_0 \approx 0.002$ m. This source was included to have a smooth transition from the refined outboard region, in the eventuality that any turbulent eddies propagate inboard. A global first cell height of 5.3×10^{-7} m gives a y^+ of around of 0.5, such that wall functions are not used.

2.3 Data Outputs and Post-Processing

The DDES was started from a partially converged steady-state solution at 3.1°. A transient phase is considered until the high eddy-viscosity regions arising from the steady RANS are eliminated, and the flow develops self-sustained unsteadiness. The total physical time simulated is 0.121 s, with statistical data recording switched on after 0.021 s. Flow-field data was sampled at a rate, f_s, of 4 kHz with a portion of the signal sampled at 20 kHz between 0.081 and 0.094 s, to investigate higher-frequency behaviour, while surface data was continuously recorded at 10 kHz. Additionally, point data was sampled at every time step (1 MHz) at 37 specific locations, 27 of which correspond to the unsteady pressure transducers on the wind tunnel model (29) and 10 points placed in the wake along two spanwise stations, at 63 and 77% span. Such sampling rates were chosen to resolve the dynamics of swept-wing buffet, namely, large-scale shock motion and associated buffet cells in the separated region. Moreover, this rich dataset allows both a phenomenal and quantitative interrogation with the high-quality BUCOLIC experimental dataset, including a direct comparison of unsteady surface pressure data measured with DPSP (19).

In addition to traditional post-processing based on pressure distributions and Fourier analysis, these massive datasets are being processed using modal analysis techniques, namely Proper Orthogonal Decomposition (POD) and Dynamic Mode Decomposition (DMD). These are purely data-based techniques which help to elucidate the flow dynamics by decomposing the input flow-field data into a set of spatio-temporal modes. POD gives a set of orthogonal modes ranked by their contribution in optimising the variance of the data, capturing the most energetic structures in the flow. Each spatial mode has a particular energy content while its behaviour in time is described by the temporal amplitudes having multiple frequencies. In contrast, DMD

Table 1
Summary of data analysed using modal analysis techniques.

Dataset	Type	Variable	f_s (kHz)	m	t_1 (s)	t_m (s)
Experimental	Surface (DPSP)	p	2	10000	0.0005	5
Numerical	Surface	p	10	1001	0.021	0.121
				906	0.0305	0.121
Numerical	Field	p, u, ρu	4	363	0.0305	0.121
Numerical	Field	p, u, ρu	20	261	0.081	0.094

identifies spatial modes each having a characteristic frequency and growth/decay rate, determined from the DMD eigenvalues. Further details are available in a recent paper outlining such techniques particularly relevant to fluid flows$^{(43)}$.

Both POD and DMD were applied to the experimental and numerical datasets using the `modred` library$^{(44)}$. The inputs are sets of vectors (commonly called snapshots), each consisting of n discrete data points at discrete times t_i, where $i = 1, \dots, m$ and m denotes the total number of snapshots. Modal decomposition was performed using the *method of snapshots*$^{(45)}$ which reduces the size of the correlation matrix, and hence the eigenvalue problem to $(m \times m)$, where $m \ll n$. Using the parallelised vector space algorithm eliminates the need to store all the snapshots in memory, enabling all the modes to be computed from the whole dataset$^{(44)}$. The snapshots are prepared in the same way for both methods, except that the temporal mean is subtracted prior to applying POD. An overview of the analysed data is provided in Table 1, including primitive and conservative variables such as static pressure p, streamwise velocity u, and streamwise momentum ρu.

3.0 RESULTS AND ANALYSIS

3.1 Steady-State Simulations

Steady-state data was first scrutinised before running the time-accurate simulation. Simulations were performed at several angles of attack between 2.0° and 3.1°, with the density residual converging to ten orders of magnitude up to 2.8°. At higher incidence angles, the residual levels out and does not converge beyond five orders of magnitude, suggesting pseudo steady states and physically unsteady flow.

The surface pressure distributions for selected angles of attack are presented in Figure 2. The surface flow visualisation is enhanced by skin friction lines whilst the boundaries of the separated region are depicted by the dotted lines. At 2.6°, a shock bubble extends from mid-span to reach the wing tip while separation at the trailing edge occurs between 70 and 89% span, the region whereby the shock is the strongest. As the incidence is slightly increased, the incipient separation at the trailing edge merges with the shock bubble at 2.7° (not shown for brevity) and the separated region starts to widen with incidence, as shown in Figure 2(*b*). This localised separated flow perturbs the shock and pushes it upstream, eventually generating spanwise oscillations visible from the shock trace at 3.1°, characteristic of a shock-buffet flow condition.

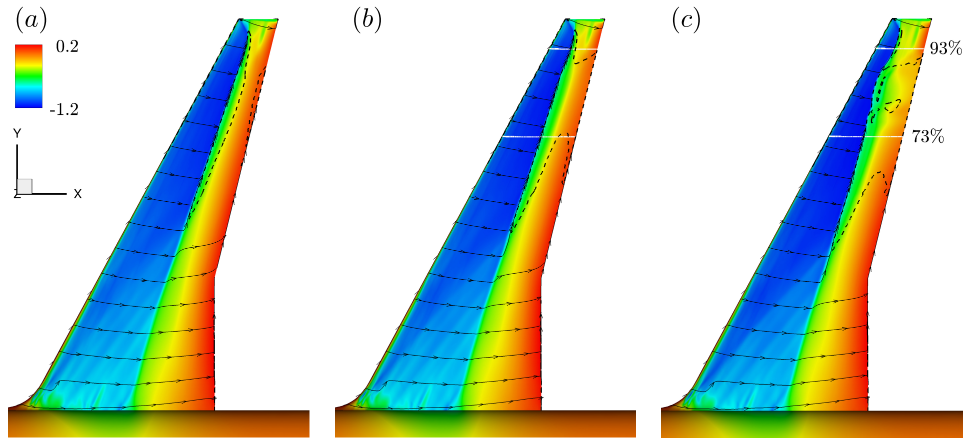

Figure 2. Surface pressure coefficient distribution highlighting skin friction lines and boundary of reversed flow region (denoted by dashed line) with increasing incidence; (*a*) 2.6°, (*b*) 2.8° and (*c*) 3.1°.

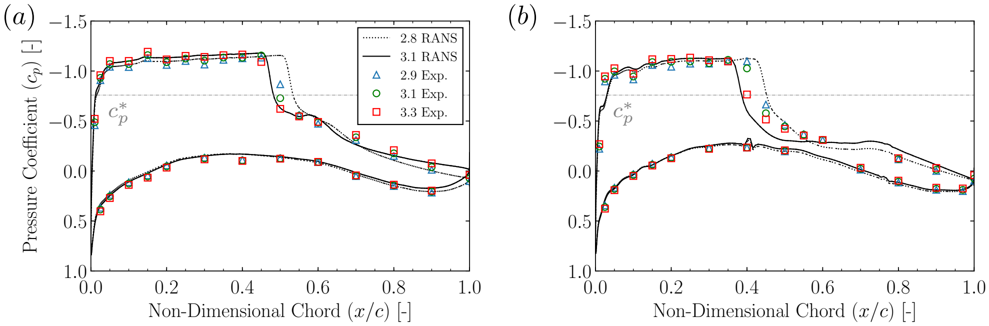

Figure 3. Chordwise pressure distributions from CFD and experimental static pressure taps at two outboard sections; (*a*) 73% span and (*b*) 93% span.

Similar observations can be drawn from the chordwise pressure distributions shown in Figure 3, at the two spanwise stations denoted by white lines in Figure 2. The critical pressure coefficient c_p^* is calculated assuming isentropic flow and taking into account the swept-wing transformation for the critical Mach number, $M_{cr} = M_\infty \cos \Lambda_{\text{LE}}$. Both pressure distributions highlight the upstream shock movement with incidence, as observed both experimentally and numerically. The 3.1° RANS distribution clearly shows the shock bubble together with the pressure divergence in the separated region downstream. The closer agreement with the higher-incidence experimental data is attributed to the effect of the flow angle, estimated to be around 0.35°, as explained in Section 2.1. Furthermore, these solutions were compared with previous work (31,32) on several different meshes, with no noticeable grid dependence.

3.2 Delayed Detached-Eddy Simulation

3.2.1 Unsteady Flow Development

One way to monitor the development of the flow unsteadiness is by studying the history of integrated values such as the lift and drag coefficients. Figure 4 presents the evo-

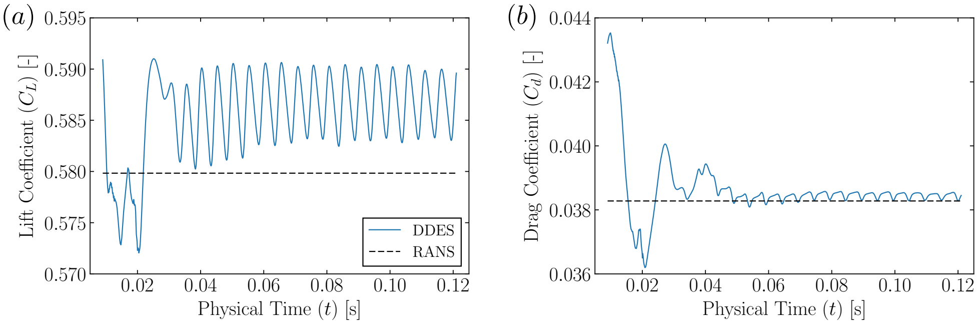

Figure 4. Time histories of the lift (a) and drag (b) coefficients obtained from the DDES. Values from the RANS solution are superimposed as reference.

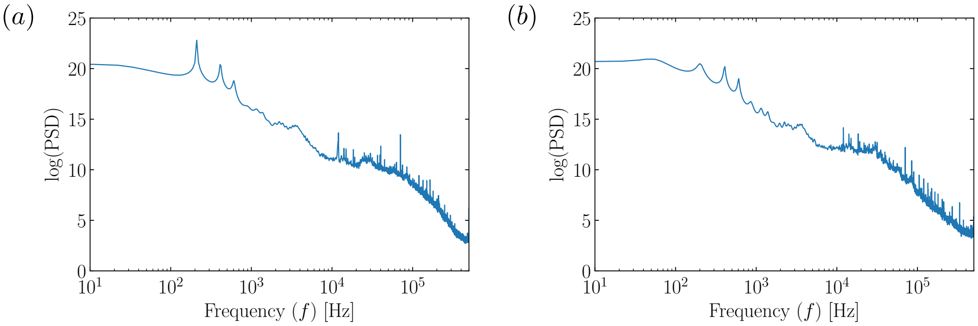

Figure 5. Power spectral density based on lift (a) and drag (b) coefficients obtained from the DDES.

lution of these coefficients as the simulation progressed. Values from the steady-state solution are also shown for comparison. Focussing on the time-accurate simulation, an initial transient phase can be observed, after which periodic, higher-frequency fluctuations corresponding to a separating and reattaching flow take place. This phase of the simulations is regarded as the onset of self-sustained shock buffet, and hence the signal ($t > 0.0305$ s) is used for the subsequent analysis, unless stated otherwise.

The power spectral densities (PSDs) of the lift and drag coefficient time histories are presented in Figure 5, computed using Burg's method(46). This autoregressive model was selected for its high frequency resolution for short signals, using an order of 4000 and a single window following a parametric study. Both plots are similar, revealing that the 200 Hz ($St = 0.2$) peak has the highest energy level. The frequency spectrum is characterised by the harmonics of these shock oscillations, which produce the biggest fluctuations of these coefficients. A broadband medium-frequency unsteadiness bump (between 2000 and 5000 Hz) is also present, which however is several orders of magnitude less energetic in terms of lift and drag coefficient fluctuation. This interpretation of low-, medium- and high-frequency unsteadiness is rooted within the context of shock-wave/boundary-layer interactions, whereby the transonic shock buffet case is an example of large-scale, low-frequency unsteadiness, since the frequencies of the shock dynamics are at least two orders of magnitude lower than the time scales associated with turbulence in the boundary layer(47,48).

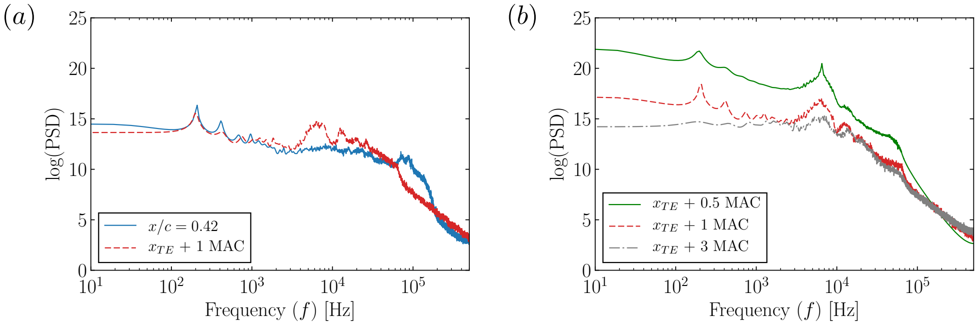

Figure 6. Power spectral density of pressure fluctuations (a) and streamwise velocity fluctuations (b) at specific points in the domain; legend gives the chordwise position, all points at 77% span.

Point data was sampled at every time step at specific locations on the wing and in the wake, in order to assess the resolution of the turbulent content. Figure 6 presents PSDs obtained from pressure and streamwise velocity data sampled at 77% span. Starting with the pressure PSD, the point on the surface at 42% chord shows a dominant peak at 200 Hz, corresponding to the shock oscillations. These fluctuations are still present in the wake at 1 MAC downstream of the trailing edge, however, the wake is characterised by a higher-frequency bump due to smaller-scale turbulent fluctuations. This broadband-frequency bump is centred at 6500 Hz and is better resolved from the velocity data. As expected, both the overall energy levels and the aforementioned peak reduce in magnitude further downstream.

It is worth to note that visualising the surface pressure snapshots during the initial transient reveals large-scale shock oscillations along the whole span that propagate towards the root. After some low-frequency oscillations, the inboard region becomes steady, whereas localised patches of separated flow on outboard sections of the wing generate self-sustained shock oscillations, which now propagate towards the tip. This behaviour is reminiscent of the wind tunnel observations. Analysis of unsteady transducer and DPSP data along the shock foot has shown that a broadband low-frequency bump centred around 70 Hz ($St = 0.07$) is present even below buffet onset conditions. This corresponds to shock unsteadiness that propagates pressure disturbances from outboard sections towards the root. At critical conditions (buffet onset), incipient separation at the trailing edge rapidly merges with the shock bubble, and the propagation along the shock reverses direction close to the wing tip. Additionally, distinct higher-frequency ($>$ 200 Hz) outboard-running waves appear beyond buffet onset (19,29).

The evolution of lift coefficient with incidence from both numerical and experimental data is shown in Figure 7. The experimental data is measured with a five-component strain-gauge balance and data both including and excluding the flow angle estimate is presented, with the former giving a better correlation with the numerical data. Steady-state numerical data tends to overestimate the lift coefficient due to a more downstream shock location. Time-accurate data from this simulation at 3.1° and a previous simulation (27) at 3.8° is depicted with a square denoting the mean, and a line showing the fluctuation range. Focussing on the current simulation, the periodic shock oscillations generate relatively small fluctuations of around ±0.05 the mean value. As highlighted in this paper, these fluctuations are due to outboard shock perturbations pertaining to the shock buffet instability, similar to the experimental observations.

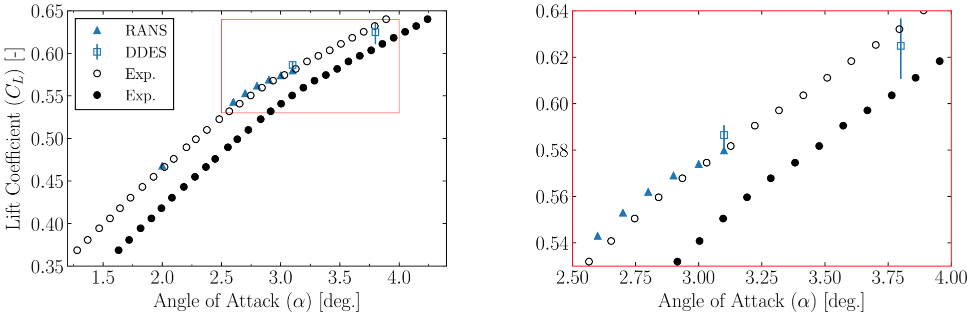

Figure 7. Comparison of lift coefficient with angle of attack from CFD (line denotes variation with time) and experiment (open symbols include the flow angle correction; filled symbols exclude it).

3.2.2 Modal Analysis

The flow field was analysed using modal analysis techniques to help elucidate the flow physics, as explained in Section 2.3. Surface pressure snapshots obtained both experimentally and numerically are first analysed, followed by analysis of the flow field over the whole computational domain.

Starting with a POD analysis of surface pressure, the spatial components of the dominant POD modes are shown in Figure 8, coloured by the spatial amplitudes. In all cases, mode 1, having the highest POD energy is related to the spanwise shock unsteadiness. Depending on the sign of the temporal amplitudes at instantaneous time steps, the spatial amplitudes represent either positive or negative pressure fluctuations. Consider a positive temporal amplitude; regions of higher and lower pressure are depicted by positive (red) and negative (blue) spatial amplitudes. Focussing on the outboard wing section, upstream shock perturbations (increased pressure behind shock in red) are associated with a region of separated flow (lower pressure in blue). Further inboard, where the flow remains attached, the shock curves outboard of the crank and adopts a downstream position. This is clear from Figures 8(a) and 8(b), showing the experimental data and the DDES data that includes part of the initial transient, respectively. As discussed previously, the inboard shock unsteadiness decays in the simulation, and any perturbations become confined to outboard sections when the transient has passed, as seen in Figure 8(c).

Figure 9 presents another POD mode for each case; mode 8 from the DPSP data and mode 2 from the DDES data. Experimentally, a number of modes capture the structural response or shock unsteadiness along the whole span(29). The mode shown is the first (in terms of POD energy) to depict the shock rippling at outboard sections, with pockets of shock-induced separation (buffet cells) which travel towards the tip. This behaviour was confirmed by animating the surface pressure snapshots and also by reconstructing the flow field using the first few dominant POD modes. The frequency spectra of the modes that have been presented are shown in Figure 10. Experimentally, there is a shift to higher frequency from the spanwise shock unsteadiness (bump centred around 70 Hz) to mode 8, depicting the outboard-running waves. Numerically, both modes 1 and 2 show a clear peak at 200 Hz corresponding to the shock oscillations. It should be noted that the PSDs have been normalised by the maximum value, whilst the PSD of the longer DPSP signal was computed using Welch's method(49).

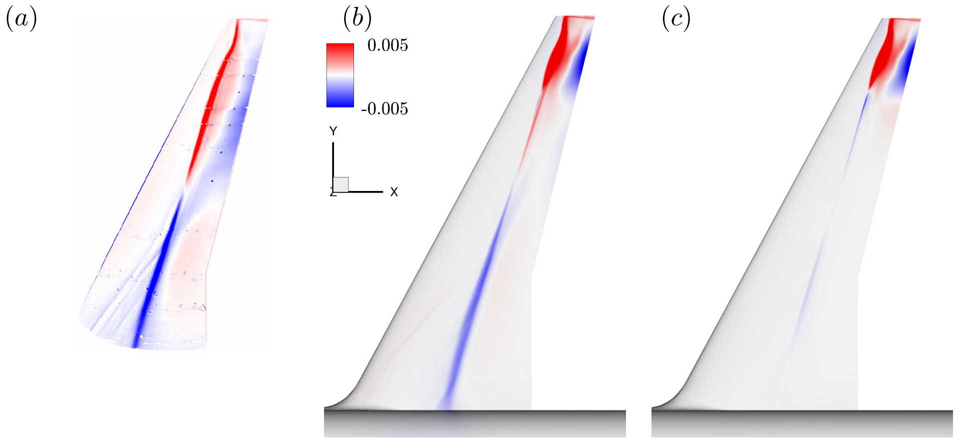

Figure 8. Dominant POD modes obtained from unsteady surface pressure data; (*a*) Experimental DPSP at 3.3°, (*b*) DDES ($0.021 \leq t_i \leq 0.121$ s) and (*c*) DDES ($0.0305 \leq t_i \leq 0.121$ s).

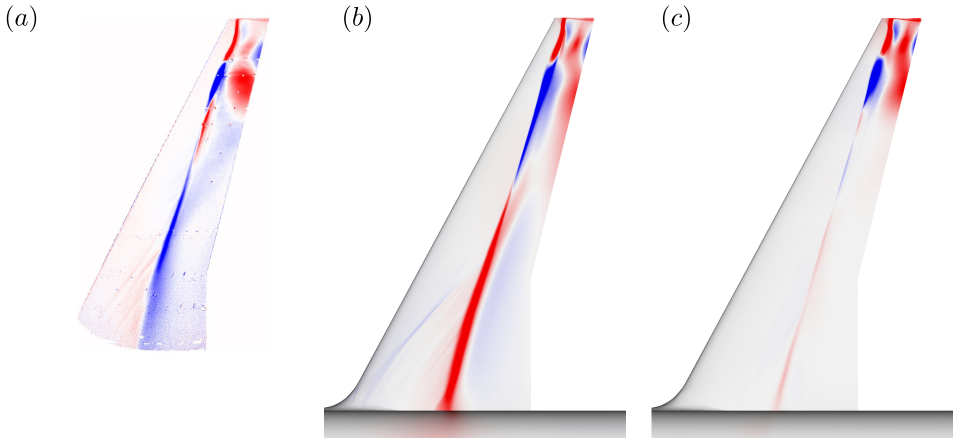

Figure 9. POD modes obtained from unsteady surface pressure data; (*a*) experimental DPSP at 3.3°, (*b*) DDES ($0.021 \leq t_i \leq 0.121$ s) and (*c*) DDES ($0.0305 \leq t_i \leq 0.121$ s).

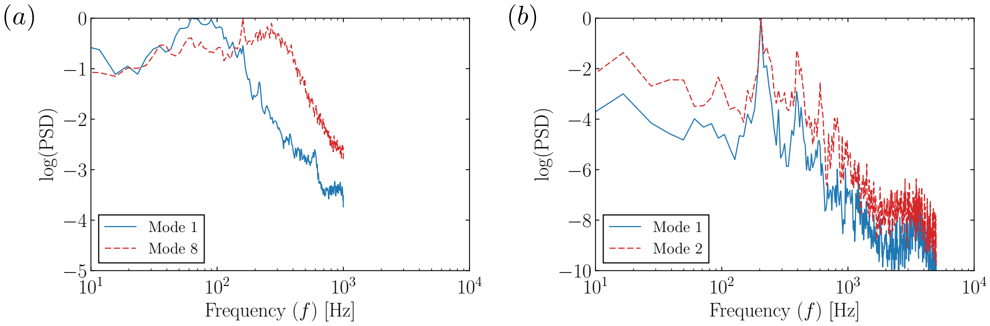

Figure 10. PSDs of POD temporal amplitudes for selected modes; (*a*) experimental DPSP (*b*) DDES.

Shifting the focus to DMD, its main advantage is that each resulting mode has a single frequency, useful to pick out dynamically important modes. However, there is no ideal way of sorting the modes, rendering mode selection challenging. One method is to scale the mode norms by the eigenvalues in order to promote growing and slowly-decaying modes(50), $|\lambda|^{m-1}||\Phi||$, where $|\lambda|$ denotes the absolute value of the complex DMD eigenvalue and $||\Phi||$ represents the DMD spectral coefficient, the biorthogonal projection of the first snapshot onto the DMD mode(44). The resulting DMD spectrum from the numerical surface pressure snapshots is presented in Figure 11. The frequency versus growth rate map gives an overview of several DMD modes, while the scaled mode norms help identify the dominant modes.

The spatial amplitudes of the dominant DMD mode are depicted in Figure 12. Having the highest scaled mode norm, this mode oscillating at 197 Hz greatly contributes to the long-term dynamics of the flow. In fact, the spatial component closely resembles the dominant POD mode in Figure 8(c), whereby the outboard separation and shock perturbations generate the biggest pressure fluctuations. More importantly, the oscillation frequency matches the peak of the lift and drag coefficient PSDs. The phase angle distribution in Figure 12(c) describes how pressure propagates on the surface based on this complex DMD mode. Apparent discontinuities are due to phase wrapping and are unphysical. Focussing on the shock foot, the phase gradually decreases in the spanwise direction outboard of around 75% span, and this corresponds to pressure propagating towards the wing tip. Furthermore, the trailing-edge separation close to the wing tip has an opposite phase with the shock foot, corroborating the flow physics implied by the opposite signs of the POD spatial amplitudes.

This behaviour is illustrated in Figure 13 by the time-dependent reconstruction of the dominant DMD conjugate pair. One period, T, assuming a 200 Hz oscillation, is shown by the insets which detail the outboard wing from 75% span. Initially, the shock sits downstream with the flow remaining attached at the trailing edge. Simultaneously, the shock has started moving forward further inboard due to a pressure perturbation. At $t/T = 0.2$, the shock continues to shift upstream inducing a trailing-edge separation due to the increased relative velocity between the shock and the flow. As the separated area widens and the shock adopts its most upstream position over a greater span ($t/T = 0.4$), the separation bubble starts to shrink, causing a downstream shock motion from further inboard ($t/T = 0.6$). The decreased local shock strength no

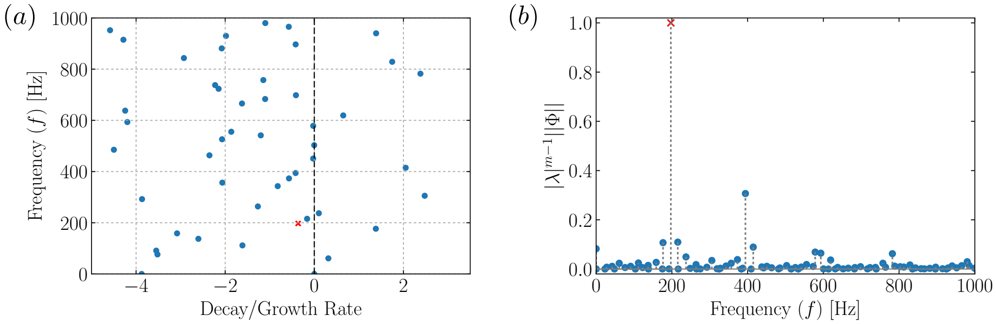

Figure 11. DMD spectrum for the numerical surface pressure snapshots, dominant mode is marked by a cross; (a) frequency versus growth rate map and (b) normalised scaled mode norms.

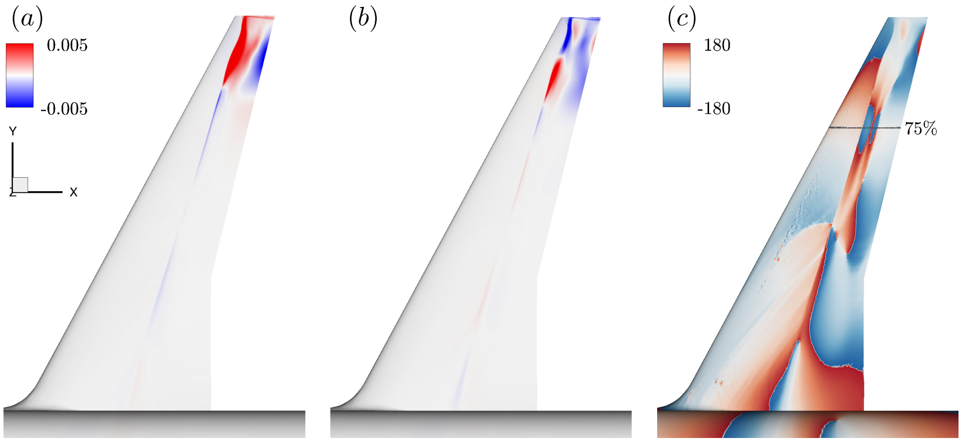

Figure 12. Dominant DMD mode ($f = 197$ Hz, decaying at 0.363 s^{-1}) from the DDES data ($0.0305 \leq t_i \leq 0.121$); (*a*) real part, (*b*) imaginary part and (*c*) phase angle (deg.).

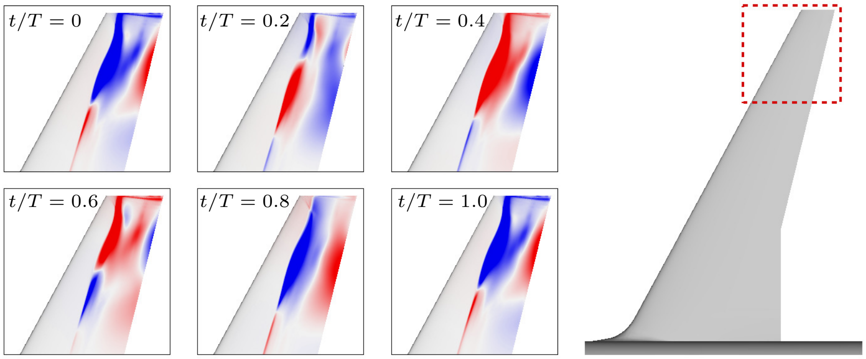

Figure 13. Reconstruction of dominant DMD mode at 197 Hz over one period, T; contours are coloured by the pressure coefficient between 0.1 (red) and -0.1 (blue), whilst instantaneous snapshots are at equal intervals of $\Delta t = 0.005$ s between $0.0305 \leq t_i \leq 0.0355$ s.

longer induces a separation ($t/T = 0.8$) until the shock starts shifting forward again and the cycle repeats ($t/T = 0 = 1$). Such span-wise shock rippling convects pressure downstream and outboard, with the spatio-temporal variation in shock strength giving rise to apparent buffet cells. Such behaviour has been reported for several swept wings both experimentally (20,21) and numerically (18,30), with a broadband signature typically between Strouhal numbers of 0.2 and 0.6. It should be emphasised that these works study flow conditions well-beyond buffet onset, characterised by non-periodic shock motion, whereas this paper details the buffet-onset region. Furthermore, a single unstable linear eigenmode linking these buffet cells and three-dimensional buffet to an absolute instability has been recently reported from a global stability analysis (23).

Other DMD modes identified by the scaled mode norms were also visualised and analysed. In general, these all show some contribution to the dynamics previously described. For instance, the second DMD mode oscillates at 394 Hz and decays

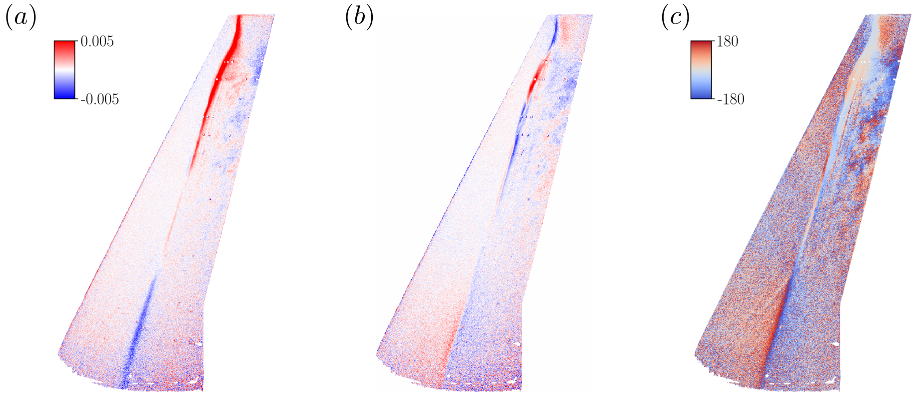

Figure 14. DMD mode ($f = 212$ Hz, decaying at 0.763 s^{-1}) from the experimental DPSP data at 3.3°; (a) real part, (b) imaginary part and (c) phase angle (deg.).

at 0.42 s^{-1}. This is the first harmonic of the dominant mode and shows finer detail and smaller-scale interactions when visualised (not shown herein for brevity). It should be noted that while a number of DMD modes have a positive growth rate in Figure 11(a), these were not picked out as dominant due to their relatively small mode norms. DMD was also applied to the DPSP dataset and resulting modes in this frequency range exhibit similar dynamics. Such a mode capturing the outboard-running waves at 212 Hz is presented in Figure 14, with such behaviour indicated by the phase angle variation and confirmed by a time-dependent reconstruction.

The modal analysis was extended to the field data. Similar flow physics constituting the shock buffet instability can be deciphered from the spatial structures of the dominant POD modes based on both pressure and velocity data, with the former shown in Figure 15. The pressure data clearly shows the radiation of pressure from the trailing-edge separation, and highlights the opposite signs between the pressure at the shock foot and at the trailing edge, as concluded from the surface analysis. Both the dominant streamwise velocity and momentum modes then highlight the separation and their perturbations extending into the wake. Temporally, dominant modes from both pressure and velocity data have the same frequency peak at 200 Hz, as shown in Figure 18(a). Similar spatial structures were obtained from a DMD analysis of the field data. Figure 16 presents the real and imaginary parts of the dominant mode oscillating at 197 Hz from the pressure data. Such a mode depicts the outboard-running waves along the shock and the progression of buffet cells towards the wing tip.

The POD analysis of the field data sampled at 20 kHz results in the same dominant modes as the lower-sampled snapshots. However, the highly-sampled segment reveals additional modes constituting coherent, spatially periodic structures in the wake, as shown by mode 39 in Figure 17. Such modes exist in pairs which are similar but shifted (90° out-of-phase), together describing the downstream convection of such eddies. Temporally, these mode pairs have a higher-frequency bump peaking at 6500 Hz (see Figure 18(b)), which is in the range of the medium-frequency bump resulting from the point data in Figure 6. Although a number of other modes also show turbulent structures and together span the whole frequency range until the Nyquist frequency, the spatial structures are random. In contrast, modes with coherent structures always have frequency spectra limited to this aforementioned bump. Both their spatial structures and the frequency content suggest that such modes are related to a Kelvin-Helmholtz-type instability, which co-exists with the shock-buffet instability further upstream. Such observations have been reported for both aerofoils (12) and wings (20) in buffeting conditions.

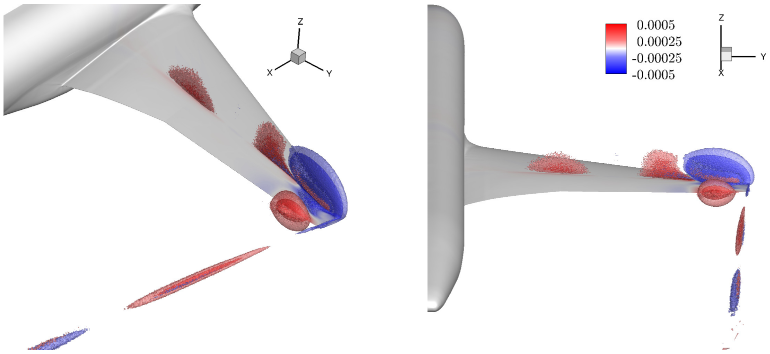

Figure 15. Spatial structure of the dominant POD mode from the field static pressure data p, visualised by iso-surfaces of the spatial amplitudes shown in the legend.

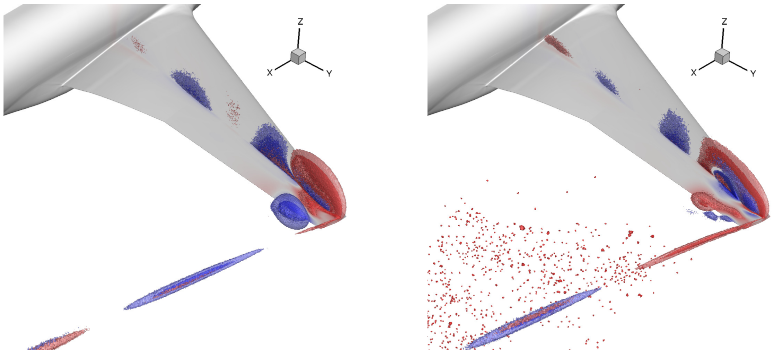

Figure 16. Real and imaginary parts of the dominant DMD mode ($f = 197$ Hz, decaying at 0.282 s^{-1}) from the field static pressure data p; iso-surfaces follow the legend in Figure 15.

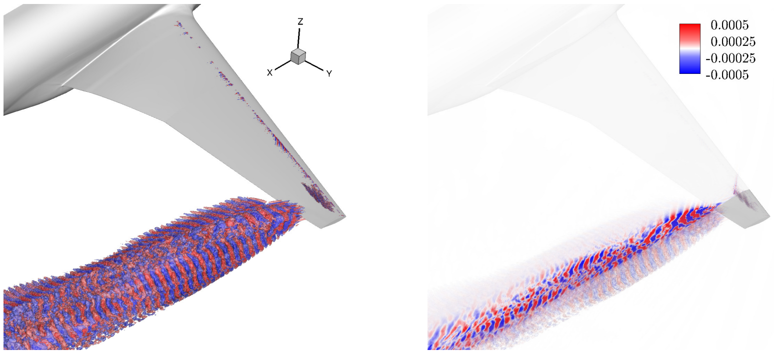

Figure 17. Spatial structure of a coherent POD mode from the streamwise velocity data u, sampled at 20 kHz, visualised by iso-surfaces of the spatial amplitudes shown in the legend; slice at 89% span.

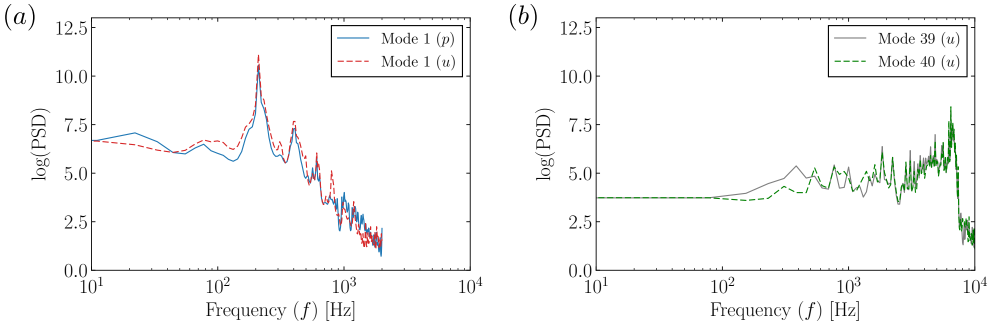

Figure 18. PSDs of POD temporal amplitudes from field data; (a) $f_s = 4$ kHz ($0.0305 \leq t_i \leq 0.121$ s) and (b) $f_s = 20$ kHz ($0.081 \leq t_i \leq 0.94$ s).

4.0 CONCLUSIONS

A delayed detached-eddy simulation of a civil aircraft wing at the design Mach number and near buffet-onset angle of attack has been presented. This approach can resolve the dynamics of swept-wing buffet, namely the low-frequency large-scale shock motion and associated buffet cells in the separated region. Once the trailing-edge separation merges with the shock bubble, the separated region periodically perturbs the shock wave and vice versa, via a self-sustaining mechanism. Such oscillations propagate pressure disturbances towards the wing tip at a Strouhal number of around 0.2.

This behaviour is confirmed by modal analysis using both proper orthogonal decomposition and dynamic mode decomposition. Dominant modes from these two methods show spatial structures describing the shock unsteadiness and separated region on the outboard section of the wing. The shock wave ripples close to the wing tip, propagating pressure perturbations in the outboard direction. Moreover, such modes have a frequency peak which matches the lift and drag oscillations. Results from modal analysis on experimental dynamic pressure-sensitive paint data confirm a similar behaviour highlighting the presence of outboard-running waves along the shock at the same characteristic frequency range.

Such a synergistic study complementing high-quality experimental and numerical data, in addition to furthering the understanding of edge-of-the-envelope flow physics, helps identify any influence from the wind-tunnel environment on the inherent dynamics of shock buffet. Finally, this paper contributes to the knowledge gap at buffet onset conditions, ultimately informing modern wing design and routes to buffet control.

ACKNOWLEDGEMENTS

This work used the ARCHER UK National Supercomputing Service (*http://archer.ac.uk*). The authors would like to acknowledge David Norman at the Aircraft Research Association Ltd. (ARA) for generating the mesh. The first author is jointly funded by ARA and the University of Liverpool.

REFERENCES

1. B. H. K. Lee, "Self-sustained shock oscillations on airfoils at transonic speeds," *Progress in Aerospace Sciences*, vol. 37, no. 2, pp. 147–196, 2001.

2. J. B. McDevitt and A. F. Okuno, "Static and dynamic pressure measurements on a NACA 0012 airfoil in the Ames high Reynolds number facility," Tech. Rep. NASA TP 2485, 1985.
3. L. Jacquin, P. Molton, S. Deck, B. Maury, and D. Soulevant, "Experimental Study of Shock Oscillation over a Transonic Supercritical Profile," *AIAA Journal*, vol. 47, no. 9, pp. 1985–1994, 2009.
4. A. Feldhusen-Hoffmann, V. Statnikov, M. Klaas, and W. Schröder, "Investigation of shock–acoustic-wave interaction in transonic flow," *Experiments in Fluids*, vol. 59, no. 15, pp. 1–13, 2018.
5. V. Brunet, "Computational Study of Buffet Phenomenon with Unsteady RANS Equations," 2003. AIAA 2003-2679.
6. Q. Xiao, H.-M. Tsai, and F. Liu, "Numerical Study of Transonic Buffet on a Supercritical Airfoil," *AIAA Journal*, vol. 44, no. 3, pp. 620–628, 2006.
7. M. Iovnovich and D. E. Raveh, "Reynolds-Averaged Navier-Stokes Study of the Shock-Buffet Instability Mechanism," *AIAA Journal*, vol. 50, no. 4, pp. 880–890, 2012.
8. S. Deck, "Numerical Simulation of Transonic Buffet over a Supercritical Airfoil," *AIAA Journal*, vol. 43, no. 7, pp. 1556–1566, 2005.
9. F. Grossi, M. Braza, and Y. Hoarau, "Prediction of Transonic Buffet by Delayed Detached-Eddy Simulation," *AIAA Journal*, vol. 52, no. 10, pp. 2300–2312, 2014.
10. A. Memmolo, M. Bernardini, and S. Pirozzoli, "Scrutiny of buffet mechanisms in transonic flow," *International Journal of Numerical Methods for Heat & Fluid Flow*, 2018. Just accepted.
11. J. Crouch, A. Garbaruk, D. Magidov, and A. Travin, "Origin of transonic buffet on aerofoils," *Journal of Fluid Mechanics*, vol. 628, pp. 357–369, 2009.
12. F. Sartor, C. Mettot, and D. Sipp, "Stability, receptivity, and sensitivity analyses of buffeting transonic flow over a profile," *AIAA Journal*, vol. 53, no. 7, pp. 1980–1993, 2014.
13. N. F. Giannelis, G. A. Vio, and O. Levinski, "A review of recent developments in the understanding of transonic shock buffet," *Progress in Aerospace Sciences*, vol. 92, pp. 39–84, 2017.
14. C. Hwang and W. S. Pi, "Northrop F-5 A aircraft transonic buffet pressure data acquisition and response analysis," *Journal of Aircraft*, vol. 12, no. 9, pp. 714–720, 1975.
15. D. Riddle, "Wind-tunnel investigation of surface-pressure fluctuations associated with aircraft buffet," 1975. AIAA 75-67.
16. F. Roos, "The buffeting pressure field of a high-aspect-ratio swept wing," 1985. AIAA 1985-1609.
17. B. Benoit and I. Legrain, "Buffeting prediction for transport aircraft applications based on unsteady pressure measurements," 1987. AIAA 87-2356.
18. M. Iovnovich and D. E. Raveh, "Numerical Study of Shock Buffet on Three-Dimensional Wings," *AIAA Journal*, vol. 53, no. 2, pp. 449–463, 2015.

19. S. Lawson, D. Greenwell, and M. K. Quinn, “Characterisation of buffet on a civil aircraft wing,” 2016. AIAA 2016-1309.
20. J. Dandois, “Experimental study of transonic buffet phenomenon on a 3D swept wing,” *Physics of Fluids*, vol. 28, no. 016101, pp. 1–17, 2016.
21. S. Koike, M. Ueno, K. Nakakita, and A. Hashimoto, “Unsteady Pressure Measurement of Transonic Buffet on NASA Common Research Model,” 2016. AIAA 2016-4044.
22. S. Timme and R. Thormann, “Towards three-dimensional global stability analysis of transonic shock buffet,” 2016. AIAA 2016-3848.
23. S. Timme, “Global instability of wing shock buffet,” *arXiv e-prints*, 2018. arXiv:1806.07299 [physics.flu-dyn].
24. P. C. Steimle, D.-C. Karhoff, and W. Schröder, “Unsteady Transonic Flow over a Transport-Type Swept Wing,” *AIAA Journal*, vol. 50, no. 2, pp. 399–415, 2012.
25. Y. Sugioka, D. Numata, K. Asai, S. Koike, K. Nakakita, and S. Koga, “Unsteady PSP Measurement of Transonic Buffet on a Wing,” 2015. AIAA 2015-0025.
26. Y. Sugioka, S. Koike, K. Nakakita, D. Numata, T. Nonomura, and K. Asai, “Experimental analysis of transonic buffet on a 3d swept wing using fast-response pressure-sensitive paint,” *Experiments in Fluids*, vol. 59, no. 108, pp. 1–20, 2018.
27. F. Sartor and S. Timme, “Delayed Detached–Eddy Simulation of Shock Buffet on Half Wing–Body Configuration,” *AIAA Journal*, pp. 1230–1240, 2016.
28. T. Ishida, A. Hashimoto, Y. Ohmichi, T. Aoyama, and K. Takekawa, “Transonic Buffet Simulation over NASA-CRM by Unsteady-FaSTAR Code,” 2017. AIAA 2017-0494.
29. L. Masini, S. Timme, A. Ciarella, and A. J. Peace, “Influence of vane vortex generators on transonic wing buffet: further analysis of the bucolic experimental dataset,” 2017. FP14-AERO2017-masini.
30. Y. Ohmichi, T. Ishida, and A. Hashimoto, “Modal decomposition analysis of three-dimensional transonic buffet phenomenon on a swept wing,” *AIAA Journal*, 2018. Just accepted.
31. F. Sartor and S. Timme, “Mach number effects on buffeting flow on a half wing-body configuration,” *International Journal of Heat & Fluid Flow*, vol. 26, no. 7, pp. 2066–2080, 2016.
32. F. Sartor and S. Timme, “Reynolds-averaged navier-stokes simulations of shock buffet on half wing-body configuration,” 2015. AIAA 2015-1939.
33. A. Probst and S. Reuß, “Scale-Resolving Simulations of Wall-Bounded Flows with an Unstructured Compressible Flow Solver,” in *Progress in Hybrid RANS-LES Modelling*, vol. 130, pp. 481–491, Springer, 2015.
34. S. R. Allmaras, F. T. Johnson, and P. R. Spalart, “Modifications and clarifications of the spalart-allmaras turbulence model,” 2012. ICCFD7-1902.
35. J. Crouch, A. Garbaruk, and D. Magidov, “Predicting the onset of flow unsteadiness based on global instability,” *Journal of Computational Physics*, vol. 224, no. 2, pp. 924–940, 2007.

36. P. R. Spalart, S. Deck, M. L. Shur, K. D. Squires, M. K. Strelets, and A. Travin, "A New Version of Detached-eddy Simulation, Resistant to Ambiguous Grid Densities," *Theoretical and Computational Fluid Dynamics*, vol. 20, no. 3, pp. 181–195, 2006.
37. A. Probst and S. Reuß, "Progress in Scale-Resolving Simulations with the DLR-TAU Code," Tech. Rep. 420051, DLR, 2016.
38. J. Löwe, A. Probst, R. Knopp, and N. Jarrin, "A low-dissipation low-dispersion second-order scheme for unstructured finite-volume flow solvers," 2015. AIAA 2015-0815.
39. A. Probst, J. Löwe, S. Reuß, and R. Kessler, "Scale-resolving simulations with a low-dissipation low-dispersion second-order scheme for unstructured finite-volume flow solvers," 2015. AIAA 2015-0816.
40. P. R. Spalart and C. Streett, "Young-person's guide to detached-eddy simulation grids," Tech. Rep. CR-2001-211032, NASA, 2001.
41. J. Shaw, S. Stokes, and M. Lucking, "The rapid and robust generation of efficient hybrid grids for rans simulations over complete aircraft," *International Journal for Numerical Methods in Fluids*, vol. 43, no. 6-7, pp. 785–821, 2003.
42. R. Rudnik, S. Melber-Wilkending, and P. Risley-Settle, "Tau-solar contributions to the 3rd high lift prediction workshop," 2018. AIAA 2018-1035.
43. K. Taira, S. L. Brunton, S. T. M. Dawson, C. W. Rowley, T. Colonius, B. J. McKeon, O. T. Schmidt, S. Stanislav, V. Theofilis, and L. S. Ukeiley, "Modal Analysis of Fluid Flows: An Overview," *AIAA Journal*, vol. 55, no. 12, pp. 4013–4041, 2017.
44. B. A. Belson, J. H. Tu, and C. W. Rowley, "Algorithm 945: Modred—A Parallelized Model Reduction Library," *ACM Transactions on Mathematical Software*, vol. 40, no. 4, pp. 1–23, 2014.
45. L. Sirovich, "Turbulence and the dynamics of coherent structures. i. coherent structures," *Quarterly of applied mathematics*, vol. 45, no. 3, pp. 561–571, 1987.
46. J. P. Burg, "Maximum entropy spectral analysis," in *37th Annual International Meeting of the Society of Exploration Geophysicists*, 1967.
47. N. T. Clemens and V. Narayanaswamy, "Low-frequency unsteadiness of shock wave/turbulent boundary layer interactions," *Annual Review of Fluid Mechanics*, vol. 46, pp. 469–492, 2014.
48. D. V. Gaitonde, "Progress in shock wave/boundary layer interactions," *Progress in Aerospace Sciences*, vol. 72, pp. 80–99, 2015.
49. P. Welch, "The use of fast Fourier transform for the estimation of power spectra: A method based on time averaging over short, modified periodograms," *IEEE Transaction on Audio and Electroacoustics*, vol. 15, no. 2, pp. 70–73, 1967.
50. J. H. Tu, C. W. Rowley, D. M. Luchtenburg, S. L. Brunton, and J. N. Kutz, "On dynamic mode decomposition: theory and applications," *Journal of Computational Dynamics*, vol. 1, no. 2, pp. 391–421, 2014.